Volume 16
Number 4
23 February 2026
Pages 1061–1476

Catalysis Science & Technology

rsc.li/catalysis

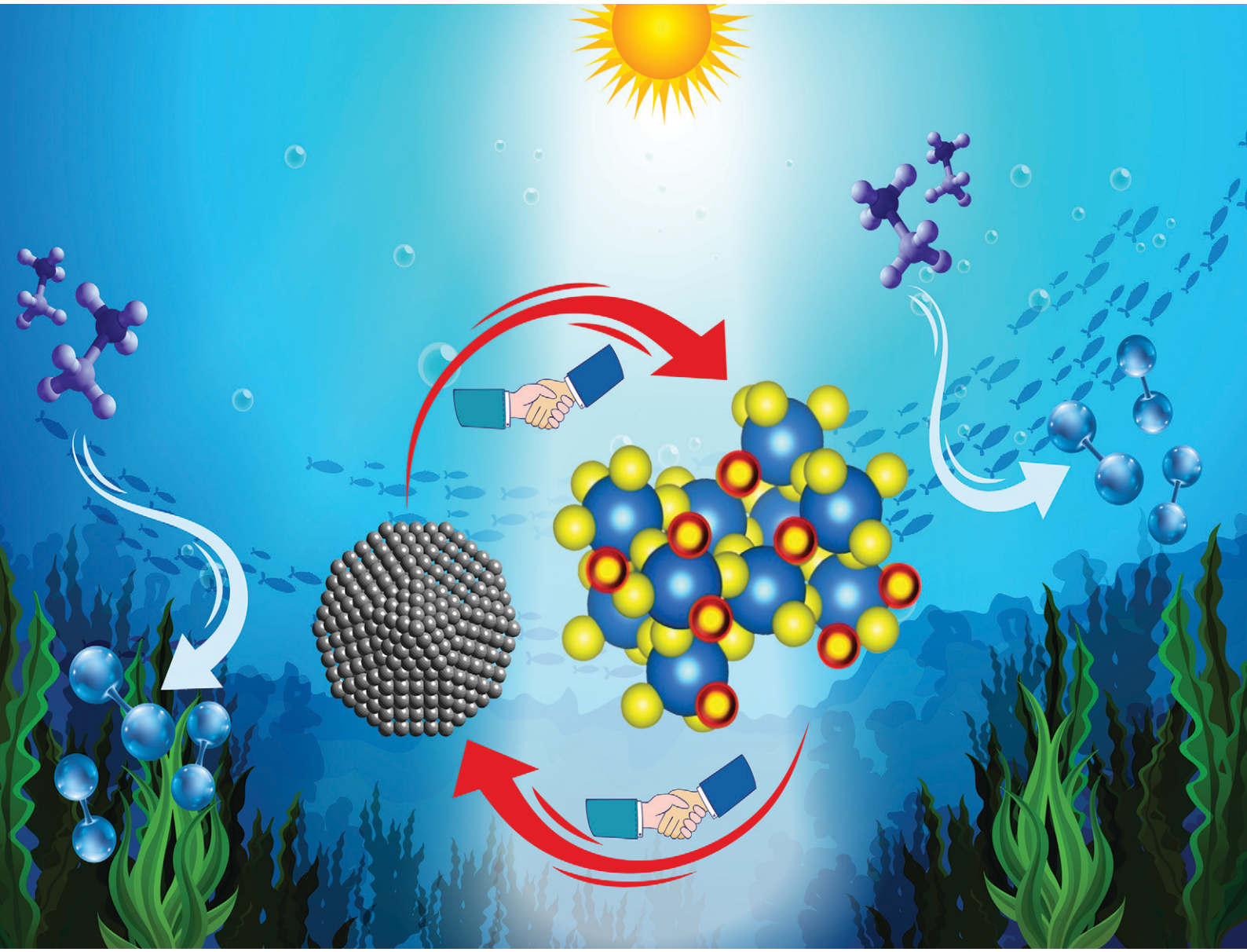

ISSN 2044-4761

ROYAL SOCIETY OF CHEMISTRY

PAPER

Priyanka Verma *et al.*

Defect-engineered Pd/WO_{3-x} nanostructures with tunable morphology for enhanced visible-NIR light-driven catalysis

Catalysis Science & Technology

ROYAL SOCIETY OF CHEMISTRY

PAPER

View Article Online
View Journal | View Issue

Cite this: *Catal. Sci. Technol.*, 2026, **16**, 1220

Defect-engineered Pd/WO_{3-x} nanostructures with tunable morphology for enhanced visible-NIR light-driven catalysis

Priyanka,[a] Rashmi,[a] Hideyuki Kawasoko,[b] Soichi Kikkawa,[b] Seiji Yamazoe,[b] Ryo Watanabe,[c] Choji Fukuhara[c] and Priyanka Verma *[a]

Semiconductor-based heterogeneous photocatalysis has garnered significant attention, showing considerable promise as a strategy for addressing problems associated with renewable energy and environmental remediation. Plasmonic semiconductors enhance photocatalysis by enabling localized surface plasmon resonance that enhances the light absorption and generates hot carriers. These carriers drive redox reactions efficiently, improving the photocatalytic performance. Herein, Pd nanoparticles (NPs) (2.5 wt%) were successfully deposited onto a non-stoichiometric form of tungsten trioxide (WO_{3-x}) with oxygen defects using a controlled morphology technique. Generating oxygen-deficient states in the WO_3 structure significantly enhanced its electronic properties, facilitating improved charge carrier separation and superior catalytic performance. The prepared catalysts were characterized using various techniques, including UV-vis spectroscopy, EPR, FT-EXAFS, HR-TEM, Mott–Schottky, XPS, and N_2 physisorption analysis. The light-driven catalytic performance of the prepared nanocatalyst was evaluated through the conversion of 4-nitrophenol (4-NP) to 4-aminophenol (4-AP), utilizing hydrogen generated *in situ* from ammonia borane (AB). A superior reaction rate of 0.75 min^{-1} was obtained for Pd colloids/WO_{3-x} catalyst, a 2.5 times enhancement in comparison to the reaction performed in dark conditions. The study demonstrates a crucial role of Pd NPs supported on WO_{3-x} and morphology-controlled photocatalytic activity. Based on scavenger experiments, a plausible reaction mechanism is suggested to explain the enhanced charge separation and photocatalytic performance. Our findings underscore the potential of WO_{3-x}-based materials with plasmonic properties in photocatalytic application reactions.

Received 8th October 2025,
Accepted 7th January 2026

DOI: 10.1039/d5cy01196e

rsc.li/catalysis

Introduction

The accelerated exhaustion of fossil energy resources is intensifying the global energy crisis while simultaneously contributing to an increase in environmental pollution.[1] Consequently, environmentally sustainable energy alternatives that do not produce greenhouse gas emissions have become increasingly important.[2] In recent years, solar energy harvesting and conversion have garnered significant scientific interest.[3] Among diverse renewable energy strategies, the direct transformation of solar energy into chemical fuels through photocatalysis has gained considerable attention as an efficient and sustainable route.[4,5] The distinctive ability of plasmon-active nanomaterials to capture light *via* localized surface plasmon resonance (LSPR) has attracted significant research interest.[6–11] Photocatalysis has emerged as a key technology in sustainability, addressing critical problems related to energy and the environment, including wastewater treatment, organic synthesis, and the generation of solar fuels.[12,13]

WO_3 is an efficient visible-light semiconductor (band gap 2.6–2.8 eV) and often outperforms TiO_2 under visible irradiation.[14] The previously reported studies have shown that WO_3 morphology strongly influences 4-NP degradation, and its photocatalytic activity can be significantly enhanced through ozonation or noble-metal deposition.[15–17] Oxygen vacancies in metal oxides are widely recognized for boosting photocatalytic performance. Introducing such vacancies into WO_3 and integrating Pd as a cocatalyst creates a synergistic enhancement, enabling plasmon-assisted charge transfer.[18–20] This work demonstrates a morphology-dependent, vacancy-engineered Pd/WO_{3-x} system, providing new insights for designing visible-NIR responsive photocatalysts for environmental applications.[21,22]

However, metal oxides exhibiting oxygen vacancies, including oxygen-deficient tungsten oxide (WO_{3-x}), molybdenum oxide

[a] *Department of Chemistry, Indian Institute of Technology Delhi, Hauz Khas, New Delhi 110016, India. E-mail: pverma@chemistry.iitd.ac.in*
[b] *Department of Chemistry, Graduate School of Science, Tokyo Metropolitan University, 1-1 Minami-Osawa, Hachioji, Tokyo 192-0397, Japan*
[c] *Department of Applied Chemistry and Biochemical Engineering, Graduate School of Engineering, Shizuoka University, 3-5-1 Johoku, Chuo-ku, Hamamatsu, Shizuoka 432-8561, Japan*

(MoO_{3-x}), and copper sulfide ($Cu_{2-x}S$) nanomaterials, have attracted considerable attention because of their distinct photoabsorption capabilities over a wide range, particularly in the near-infrared region.[23–27] These materials are highly promising for diverse applications due to their capability to harness vis-NIR light efficiently.[28] In semiconductor-based systems, incident light induces the generation of excited electron and hole pairs, facilitating various photochemical processes.[29] Specifically, non-stoichiometric tungsten oxide ($WO_{2.72}$) has emerged as a diverse material with applications in smart window technologies, electrochromic devices, photothermal therapy, and NIR radiation shielding, highlighting its multifunctional utility in both energy and biomedical fields.[30] The various crystalline forms of tungsten oxide, including the monoclinic $W_{18}O_{49}$ phase, have garnered significant attention owing to their characteristic defect-abundant crystal lattice.[7,31,32] WO_{3-x} serves as a promising host for LSPR, attributed to its unique electronic structure, particularly the presence of outer *d*-valence electrons. The non-stoichiometric nature of WO_{3-x}, attributed to a high density of oxygen vacancies, plays a crucial role in modulating its electronic properties. These vacancies effectively reduce the band gap, thereby enhancing the optical response.[32] Among the various mechanisms of plasmonic photocatalysis, including both direct and indirect, our research primarily centres on the direct photocatalytic pathway where the semiconductor acts as an efficient light absorber, and the co-catalyst (Pd) acts as a catalytically active site.[33]

Herein, we have reported the synthesis of Pd/WO_{3-x} nanocatalyst with varied morphologies, including nanorods, sheets, and blocks, exhibiting light-induced plasmonic excitation across the visible and near-infrared (NIR) wavelength range. Tailoring the morphological features of photocatalytic materials plays a critical role in optimizing their surface area, active site availability, light-harvesting efficiency, and charge carrier dynamics. This work highlights the effect of specific morphologies of WO_{3-x} on enhancing the plasmonic interactions, improving photogenerated charge separation, and ultimately leading to superior photocatalytic activity. The Pd deposited WO_{3-x} hybrids were synthesized *via* two distinct approaches: impregnation of a colloidal solution of Pd NPs onto WO_{3-x} support, and one-pot solvothermal synthesis. The WO_{3-x} support was synthesized *via* the solvothermal method using tungsten hexachloride (WCl_6) as the precursor. The resulting Pd/WO_{3-x} hybrid nanocatalysts demonstrated outstanding performance in the catalytic hydrogenation of 4-NP to 4-AP, under both light irradiation and dark conditions. Additionally, the influence of polyvinylpyrrolidone (PVP) as a surfactant during synthesis was examined, revealing its impact on the morphology, structural characteristics, and catalytic efficiency of the hybrids. This work introduces a novel strategy for designing plasmonic photocatalysts by integrating Pd NPs with oxygen-deficient sites in WO_{3-x} to enhance the catalytic performance under visible-NIR illumination. The insights gained from this study contribute to a broader understanding of defect engineering in plasmon-enhanced photocatalysis and offer a potential route towards advancing nano-catalysts for environmentally friendly and sustainable applications.

Experimental section

Materials

Tungsten chloride (WCl_6) was purchased from Tokyo Chemical Industry. Commercial tungsten oxide (WO_3), polyvinylpyrrolidone (PVP), and palladium acetate [$Pd(OAc)_2$] were supplied by Sigma-Aldrich Co. 4-nitrophenol ($NO_2C_6H_4OH$) and ammonia borane (NH_3BH_3) were supplied by Merck Chemicals. Ethanol (C_2H_5OH) received from Changshu Hongsheng Fine Chemical Co. Ltd. DMSO (Dimethyl sulfoxide) purchased from Actylis Pharma India Pvt. Ltd. IPA (isopropyl alcohol) was supplied by Avantor Performance Materials India Pvt. Ltd. The reagents were used directly without pre-treatment or purification.

Synthesis procedure of WO_{3-x}

Sub-stoichiometric WO_{3-x} nanostructure was synthesized using a solvothermal approach, as reported in the literature.[31] 500 mg tungsten hexachloride (WCl_6) was dissolved in 100 mL of ethanol under constant stirring until the solution turned blue, indicative of the formation of reduced tungsten species. The resulting solution was poured into a Teflon-lined stainless-steel autoclave and heated at 180 °C for 24 hours. Afterwards, the autoclave was allowed to cool down to room temperature. The resulting blue precipitate was collected *via* centrifugation and repeatedly washed with deionized water to remove any remaining impurities. The purified product was then dried at 60 °C overnight, yielding a blue WO_{3-x} powder.

Synthesis procedure of Pd/WO_{3-x} *via* the impregnation method

Palladium NPs (2.5 wt%) were loaded onto the as-synthesized WO_{3-x} support through an impregnation technique followed by hydrogen reduction. In a typical procedure, WO_{3-x} was uniformly suspended in 50 mL of ethanol to which a 5 mM palladium(II) acetate [$Pd(OAc)_2$] solution was added under continuous magnetic stirring. The mixture was continuously stirred for 4 hours to ensure uniform distribution of the Pd precursor. Subsequently, the solvent was removed using a rotary evaporator. The obtained solid was then subjected to thermal reduction in a tubular furnace under a 5% H_2 and 95% N_2 gas flow at 200 °C for 3 hours. The final product was designated as Pd/WO_{3-x}. The preparation of Pd colloids was performed following an established procedure detailed in Fig. S1 of the SI.[34–36] The Pd colloids were then impregnated on the WO_{3-x} support and labelled as Pd colloids/WO_{3-x}.

Synthesis of Pd–WO_{3-x} *via* the solvothermal method

Palladium NPs (2.5 wt%) were supported on WO_{3-x} *via* a solvothermal synthesis followed by hydrogen reduction. WCl_6 was suspended in 100 mL of ethanol, followed by adding a 5 mM solution of palladium(II) acetate [$Pd(OAc)_2$] under

continuous magnetic stirring. The prepared mixture was transferred to a stainless-steel vessel lined with Teflon and treated solvothermally at 180 °C for 24 hours. After cooling to room temperature, the solid was separated using centrifugation and thoroughly rinsed with distilled water and ethanol to eliminate any impurities. The dark brown product was dried overnight at a temperature of 60 °C. At last, the dried powder was reduced under a H_2/N_2 (5/95%) atmosphere at 200 °C for 3 hours to prepare the Pd-supported WO_{3-x} catalyst. The prepared sample was labelled as Pd-WO_{3-x}-S. The Pd-WO_{3-x}-S (PVP) was also prepared following the same procedure using a mass ratio of 0.6 : 1 for polyvinylpyrrolidone (PVP) to tungsten hexachloride (WCl_6).

Characterization

Diffuse reflectance UV-vis measurements were carried out using a JASCO V-770 UV-vis-NIR spectrophotometer to analyze the optical properties of the samples. Structural characterization was performed by recording powder X-ray diffraction (XRD) patterns on a Bruker D8 Advance diffractometer utilizing Cu Kα radiation (λ = 1.54178 Å) in continuous scanning mode. Morphological features were investigated through SEM analysis with a Hitachi tabletop instrument, while transmission electron microscopy (TEM) analysis was conducted using a JEOL JEM-1400 microscope to capture high-resolution images. The high-resolution transmission electron microscopy (HR-TEM) was performed on a JEM-ARM200F NEOARM electron microscope operating at an electron voltage of 200 keV. The reduction reaction of 4-NP to 4-AP was monitored *via* an Agilent Cary 60 spectrophotometer. X-ray photoelectron spectroscopy (XPS) was conducted using a Kratos Axis Supra system equipped with Al Kα radiation, with reference to the C 1s peak at 285 eV. Electron paramagnetic resonance (EPR) spectra were obtained at room temperature using a Bruker A300 spectrometer. Thermogravimetric analysis (TGA) was carried out on a Perkin Elmer SII instrument, applying a heating rate of 10 °C per minute. The Mott Schottky analysis was performed in a three-electrode system with FTO-supported working electrode, Pt counter, Ag/AgCl reference, in 0.5 M Na_2SO_4 electrolyte, with an AC potential frequency of 1 kHz under dark conditions using a Zahner workstation with model PP211. Specific surface area and porosity were evaluated using the BELSORP-MaxII analyzer (Microtrac BEL Corp) at liquid nitrogen temperature (−196 °C). X-ray absorption fine structure (XAFS) measurements at the W L_3- and Pd K-edges were performed in transmission mode at SPring-8 of Japan Synchrotron Radiation Research Institute in Japan, utilizing ionization chambers as detectors. Data processing was completed using xTunes software.[37]

Photocatalytic reaction

A 7 mM aqueous solution of 4-nitrophenol was used as a stock solution in the reaction. An aliquot of 10 mL from this solution was added to a glass reactor equipped with a magnetic stir bar. Subsequently, 5 mg of powdered catalyst was added to the reactor. The nitrogen gas was bubbled into the reactor system for 15 min to establish an inert environment. A freshly made aqueous solution of AB (0.025 M) was obtained *via* dissolving 7.7 mg AB in 10 mL of distilled water. The reduction reaction was initiated by introducing the AB solution into the reactor through the rubber septum. After the addition of AB, the color of the 4-NP solution immediately changed, indicating the formation of the 4-nitrophenolate ion. The reaction was monitored by withdrawing 1 mL aliquots of the reaction mixture at specific time intervals. The absorbance was measured at 400 nm and 296 nm, corresponding to nitrophenolate ion and 4-AP, respectively. The influence of light irradiation on catalytic performance was examined by evaluating the reaction under both illuminated and dark conditions. The source of light irradiation was a 300 W Xenon arc lamp (Newport).

Results and discussion

XRD analysis

Fig. 1(a and b) depicts a schematic representation of the synthesis procedure used to prepare the photocatalysts *via* the solvothermal and impregnation approach. X-ray diffraction (XRD) measurements were performed for the synthesized materials to determine their crystal structure and assess phase purity. As represented in Fig. 1(c), XRD analysis confirmed that the prepared samples consisted of a monoclinic phase, consistent with standard data for $W_{18}O_{49}$ (JCPDS No. 71-2450).[31] The diffraction peaks associated with the (010) plane, with 2θ values of 23°, were found in all samples, indicating that $W_{18}O_{49}$ likely grows in the (010) direction.[31] The sharpness and intensity of the peaks also

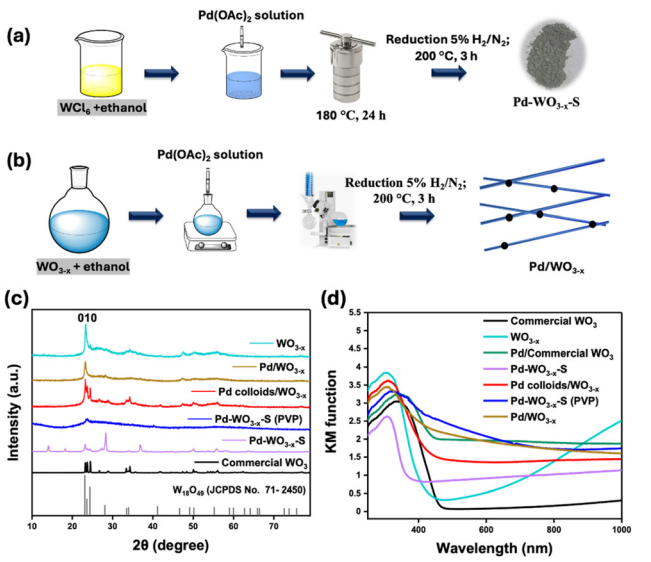

Fig. 1 (a) Schematic illustration of the photocatalyst synthesis procedure *via* solvothermal and (b) impregnation method; (c) X-ray diffraction (XRD) spectra and (d) UV-vis absorption spectra of commercial WO_3, WO_{3-x}, and Pd-decorated WO_{3-x} samples.

suggest good crystallinity of the materials. The Pd/WO_{3-x} retains the characteristic sharp and strong (010) reflection of WO_{3-x}. No distinct peaks for Pd were detected in the Pd-loaded WO_{3-x} samples, which could be attributed to the small amount of Pd used or its even distribution on the surface. There are some impurity peaks in the XRD pattern of Pd colloids/WO_{3-x}, probably due to the surfactants used in the colloidal suspension. The XRD pattern of Pd-WO_{3-x}-S suggests nanostructures grow along more than one direction. For the Pd-WO_{3-x}-S (PVP), the XRD patterns show further suppression of the (010) peak and overall reduced intensity, likely due to the introduction of surfactant (PVP), which affects nucleation and growth kinetics, leading to smaller crystallites or more amorphous structures. The progressive reduction in peak intensity and broadening from commercial WO_3 to Pd-deposited WO_{3-x} samples reflects the increasing disorder and nanoscale nature of the materials.[38]

The synthesized WO_{3-x} nanowires appeared blue when dispersed in ethanol, indicating their unique optical properties. Fig. 1(d) shows the optical profile of WO_{3-x}-based catalysts, exhibiting absorption from the visible to the near-infrared range, due to the collective excitation of free electrons attributed to the existence of oxygen vacancies along the interface, leading to LSPR.[29] It is well known that oxygen-deficient sites in metal oxides are tuned to affect the LSPR behavior.[39] The commercial WO_3 also showed negligible absorption. The Pd-decorated WO_{3-x} composites show comparatively weaker absorption than WO_{3-x}. These findings indicate that surface oxygen vacancies potentially facilitate the nucleation of Pd NPs. The Pd deposition on WO_{3-x} interferes with the light absorption by WO_{3-x}, leading to reduced intensity.[40] Among the Pd-modified samples, Pd-WO_{3-x}-S (PVP) demonstrates the highest absorption intensity across the visible region (350–700 nm). In contrast, the surfactant-free sample Pd-WO_{3-x}-S exhibits lower absorption intensity, indicating limited surface modification. The Pd colloids/WO_{3-x} and Pd/WO_{3-x} samples also show improved visible light absorption compared to commercial WO_3, though to a lesser extent than Pd-WO_{3-x}-S (PVP). Conversely, Pd/commercial WO_3 shows only marginal improvement over the unmodified WO_3, suggesting that Pd alone, without accompanying oxygen deficiency or structural modification, is insufficient to alter the optical properties significantly. To justify the origin of LSPR in WO_{3-x}, the UV-vis-NIR absorption spectra of WO_{3-x} show a broad visible-NIR absorption peak originating from vacancy-induced free carriers, unlike stoichiometric WO_3. Overall, it was revealed that both oxygen deficiency and the method of Pd incorporation play critical roles in tuning the visible and near-infrared absorption properties of WO_3-based nanomaterials.

Morphology analysis

The SEM and TEM analyses were conducted to examine the morphological features of the synthesized samples, as displayed in Fig. 2 and 3. The SEM analysis of commercial WO_3, as demonstrated in Fig. 2(a), revealed a mixture of different morphologies (cubic, spherical, and cuboidal) without a well-defined structural pattern. In contrast, Fig. 2(b and c) displays the SEM micrographs of WO_{3-x} with nanorod-like structures. Additionally, Pd-WO_{3-x}-S (PVP) in Fig. 2(d) exhibits a smooth block-like morphology. Fig. 2(e and f) depicts the morphology of Pd-WO_{3-x}-S with a sheet-like morphology. The SEM images of Pd colloids/WO_{3-x} in Fig. 2(g and h) show a spherical shape. The SEM images of Pd/WO_{3-x} and Pd/Commercial WO_3 are displayed in Fig. S2. The TEM images of WO_{3-x} in Fig. 3(a) further confirmed the formation of nanowires with high aspect ratios, lengths ranging from hundreds of nanometres to several micrometers. The TEM micrographs of Pd/WO_{3-x}, Pd-WO_{3-x}-S, Pd colloids, Pd colloids/WO_{3-x}, and Pd-WO_{3-x}-S are shown in Fig. 3(b–h). The TEM image of Pd colloids/WO_{3-x} revealed that Pd NPs were anchored on the nanowires. The HR-TEM images in Fig. 3(i–l) reveal clear lattice fringes with a 0.378 nm spacing corresponding to the (010) plane of WO_{3-x}.[41] The SAED pattern shows distinct diffraction spots/rings, confirming the polycrystalline nature of WO_{3-x}.

The N_2 adsorption–desorption isotherms for the synthesized samples are displayed in Fig. 4(a). The adsorption isotherms of all samples corresponded to type IV,

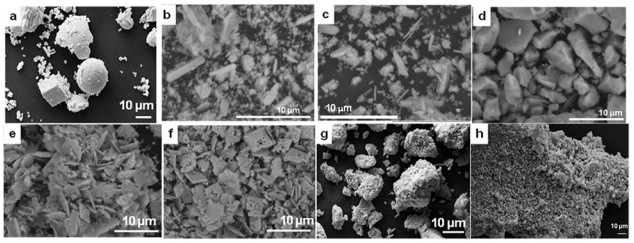

Fig. 2 (a) SEM image of commercial WO_3, (b and c) WO_{3-x}, (d) Pd-WO_{3-x}-S (PVP), (e and f) Pd-WO_{3-x}-S, and (g and h) Pd colloids/WO_{3-x}.

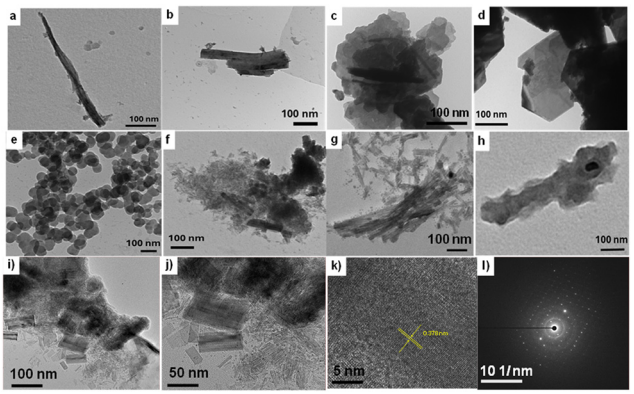

Fig. 3 TEM images of (a) WO_{3-x}, (b) Pd/WO_{3-x}, (c and d) Pd-WO_{3-x}-S (e) Pd colloids, (f and g) Pd colloids/WO_{3-x}, and (h) Pd-WO_{3-x}-S (PVP), (i and j) HR-TEM images of Pd colloids/WO_{3-x}, (k) lattice fringes with 0.378 nm *d*-spacing, and (l) corresponding SAED pattern of Pd colloids/WO_{3-x}.

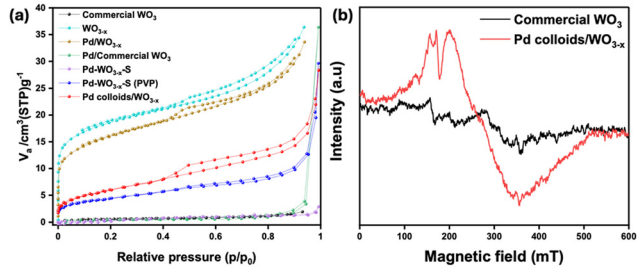

Fig. 4 (a) Nitrogen adsorption–desorption isotherm of synthesized samples (b) EPR spectra of commercial WO_3, Pd colloids/WO_{3-x} measured at room temperature conditions.

which features mesoporous structures except commercial WO_3 and Pd-WO_{3-x}-S. The determined surface area and total pore volume were evaluated through the Brunauer–Emmett–Teller (BET) and Barrett–Joyner–Halenda (BJH) methods, with detailed values summarized in Table S1. The Pore size distribution is shown in Fig. S3 (a), confirming that the pores range from 2 to 50 nm, further supporting the mesoporous features of the materials. The WO_{3-x} sample exhibits a significantly higher specific surface area of 66.51 $m^2\ g^{-1}$, 30 times higher in comparison to commercial WO_3 (2.03 $m^2\ g^{-1}$), indicating a substantial increase in available active sites. This enhancement is expected to improve both photocatalytic efficiency and adsorption capacity, owing to the increased accessibility of reactant molecules. After Pd deposition, the BET surface areas of Pd/WO_{3-x} and Pd colloids/WO_{3-x} were reduced to 56.83 $m^2\ g^{-1}$ and 22.2 $m^2\ g^{-1}$, respectively. This decrease is attributed to the partial occupancy of surface sites with Pd NPs, thus confirming the successful loading of Pd. The samples synthesized *via* the solvothermal method, Pd-WO_{3-x}-S (5.9 $m^2\ g^{-1}$) and Pd-WO_{3-x}-S (PVP) (8.0 $m^2\ g^{-1}$), exhibited significantly lower surface areas than Pd/WO_{3-x} prepared *via* impregnation. This reduction can be attributed to the dense particle aggregation and limited porosity often associated with solvothermal synthesis, especially in the presence of polymeric surfactants such as PVP.

To examine the existence of paramagnetic centres and oxygen vacancies in Pd colloids/WO_{3-x}, electron paramagnetic resonance (EPR) analysis was performed, as shown in Fig. 4(b).[42,43] The commercial WO_3 sample displayed a broad and relatively weaker EPR signal, indicating a lower concentration of unpaired electrons and minimal oxygen vacancies. A signal observed around $g \approx 2.00$ is probably associated with W^{5+} centres or isolated oxygen-deficient defects. In contrast, Pd colloids/WO_{3-x} show a stronger EPR signal, indicating abundant oxygen vacancies and unpaired electrons, compared to commercial WO_3. The EPR spectrum of Pd/WO_{3-x}, Pd-WO_{3-x}-S, and Pd-WO_{3-x}-S (PVP) is displayed in Fig. S3 (b). The Pd/WO_{3-x} exhibited a stronger EPR signal, suggesting a larger amount of oxygen vacancies, which probably trap electrons and form W^{5+} species. There may also be some contribution from palladium species in specific oxidation states, although palladium is typically EPR-silent unless under certain conditions.[42] The asymmetry and splitting of the signal point toward possible interactions between Pd and defect centres within WO_{3-x}. The Pd-WO_{3-x}-S, Pd-WO_{3-x}-S (PVP) shows enhanced electron delocalization or more isolated paramagnetic centres, confirming the preservation of oxygen vacancies following the incorporation of Pd NPs.

Thermal decomposition characteristics of the materials were evaluated using thermogravimetric analysis (TGA).[42,44–46] The inert atmosphere (N_2) was maintained during the measurements, with the temperature ramped at 10 °C min^{-1}, as illustrated in Fig. S4(a). The commercial WO_3 sample exhibited minimal weight loss up to 700 °C, indicating excellent thermal stability. In contrast, WO_{3-x} showed a weight loss of approximately 10% below 300 °C, likely due to the evaporation of residual solvents.[47] The Pd-WO_{3-x}-S (PVP) exhibited the highest weight loss (~35%) throughout the temperature range of 100–450 °C, primarily due to thermal decomposition of PVP, which was used as a surfactant during synthesis. Similarly, the Pd colloids/WO_{3-x} demonstrated a weight loss of around 10% between 100 °C and 300 °C, resulting from residual PVP decomposition, while still maintaining good thermal stability beyond 350 °C. The Pd-WO_{3-x}-S sample, synthesized without surfactant, exhibited a lower weight loss (~5%) mainly below 250 °C, possibly resulting from desorption of moisture. The Pd/Commercial WO_3 sample showed a slight weight loss of approximately 2–3% at 250 °C.

Subsequently, various characterizations were conducted to explore the electronic properties of the synthesized materials. Fig. S4(b) presents the FT-IR (Fourier-transform infrared) spectra of commercial WO_3, WO_{3-x}, and Pd-deposited samples. In commercial WO_3, distinct absorption bands were observed (800–900 cm^{-1}), which are typically ascribed to W–O–W stretching vibrations in a well-ordered WO_6 octahedral network.[47] In contrast, WO_{3-x} displayed noticeable changes in the intensity and position of these bands, suggesting structural modifications associated with the introduction of oxygen vacancy. These spectral differences confirm the surface modifications in WO_{3-x} compared to the commercial WO_3.[44,48] The peak observed around 2850–2950 cm^{-1} indicates the stretching vibrations associated with the PVP.

The Mott–Schottky curves ($1/C^2$ *vs.* V) shown in Fig. S5(a) were performed for commercial WO_3, WO_{3-x}, and Pd colloids/WO_{3-x}, exhibiting positive slope, confirmed their n-type semiconducting nature.[49] The flat-band potentials (approximating the conduction band edge) were obtained by linearly extrapolating the curve to the voltage X-axis. Commercial WO_3 shows an E_{CB} (conduction band edge potential) of approximately −0.11 V, while WO_{3-x} exhibits a slightly less negative E_{CB} of −0.02 V *vs.* Ag/AgCl.[50] Notably, Pd colloids/WO_{3-x} displays a significantly shifted conduction band edge at −0.99 V, indicating enhanced electron density and strong electronic interaction between Pd and WO_{3-x}.[51] The Tauc plots ($(\alpha h\nu)^{1/2}$ *versus* photon energy ($h\nu$)), shown in Fig. S5(b), confirm indirect band-gap transitions for commercial WO_3, WO_{3-x}, and Pd colloids/WO_{3-x}. Commercial WO_3 exhibits an optical band gap of approximately 2.58 eV,

whereas WO_{3-x} displays a reduced band gap of about 2.45 eV, consistent with the formation of oxygen-vacancy defect states that extend light absorption into the visible region. The Pd colloids/WO_{3-x} composite shows a further decrease in the band gap to around 1.64 eV, along with enhanced sub-band-gap absorption, indicating the introduction of additional electronic states and strong metal–semiconductor interactions that promote improved light harvesting and facilitate interfacial charge-transfer processes.

XPS analysis

X-ray photoelectron spectroscopy (XPS) was utilized to determine the surface chemical environment of Pd-deposited WO_{3-x} nanomaterial. The obtained W 4f and Pd 3d spectra for Pd colloids/WO_{3-x} are shown in Fig. 5(a and b), respectively. This study concentrated on the elements W, O, and Pd to analyze the variations in oxidation states and verify the existence of oxygen vacancies.[38,52] XPS also helps in examining how Pd NPs interact with the WO_{3-x} surface and how defect engineering affects the electronic structure of the nanomaterial.[42,44] The two characteristic peaks emerged at 37.7 eV (W $4f_{5/2}$) and 35.5 eV (W $4f_{7/2}$), corresponding to W^{6+}, which is characteristic of stoichiometric WO_3. Additionally, a second set of peaks at slightly lower binding energies was observed, attributed to W^{5+} species, suggesting oxygen deficiency within the lattice and the formation of non-stoichiometric WO_{3-x}. The peak area ratio of W^{6+}/W^{5+} was found to be 9.99. The Pd 3d XPS spectrum displays two prominent peaks at binding energies of 335.4 eV and 340.7 eV, corresponding to Pd $3d_{5/2}$ and Pd $3d_{3/2}$, respectively. These peaks exhibit the characteristic spin–orbit splitting of 5.3 eV and are associated with metallic palladium (Pd^0). The XPS spectrum of commercial WO_3, WO_{3-x}, and Pd/WO_{3-x} is shown in Fig. S6. The Pd 3d XPS spectra of the solvothermal samples (Pd-WO_{3-x}-S and Pd-WO_{3-x}-S-PVP) shown in Fig. S7 reveal relatively very low-intense signals of Pd, indicating that Pd is not on the surface but likely trapped within WO_{3-x}. Overall, the XPS study confirms the successful deposition of palladium within the WO_{3-x} matrix and reveals a mixed valence state of both W and Pd.

X-ray absorption spectroscopy (XAS)

To analyze the coordination environment, XAS analyses were carried out at the W L_3-edge and Pd K-edge, revealing key insights into metal-support interactions.[42,53,54] Fig. 6(a and c) presents the normalized W L_3-edge XANES and FT-EXAFS spectra of the reference WO_3 sample and the Pd-loaded WO_3-based catalysts. All samples exhibited spectral features comparable to WO_3, confirming the predominance of W(VI). Notably, variations in the intensity of the white line were observed. The reference WO_3 displayed a broad white-line peak with a characteristic plateau. In contrast, other WO_{3-x} samples showed narrower peaks shifted slightly toward lower energy with enhanced intensity, indicating distortions in the local coordination environment of W. Such distortions are typically associated with oxygen vacancies in non-stoichiometric WO_3. Importantly, no appreciable changes in XANES were observed upon Pd loading.

The Pd K-edge XANES and FT-EXAFS of the prepared samples are shown in Fig. 6(b and d) along with the reference Pd foil and PdO. All samples exhibited absorption features closely resembling metallic Pd foil, confirming that Pd predominantly exists in the metallic state. However, Pd colloids/WO_{3-x} and Pd-WO_{3-x}-S (PVP) displayed slight deviations in white-line intensity compared to Pd foil, suggesting partial oxidation of Pd. The absence of distinct PdO-like features in other samples indicates a stable metallic Pd environment. These findings confirm that the co-catalyst maintains its metallic state, with minor oxidation effects.

Evaluation of photocatalytic performance

4-Nitrophenol (4-NP) is a toxic organic contaminant frequently detected in industrial and agricultural wastewater, resulting in environmental and health concerns. In contrast, an important chemical intermediate, 4-aminophenol (4-AP), is widely utilized in the production of pharmaceuticals like analgesics and antipyretics, as well as dyes, polymers, and natural products.[55] Several treatment methods, including oxidation, degradation, adsorption, and coagulation, have been developed to remove or convert 4-NP.[56,57] To address these issues, greener and more efficient methods are being

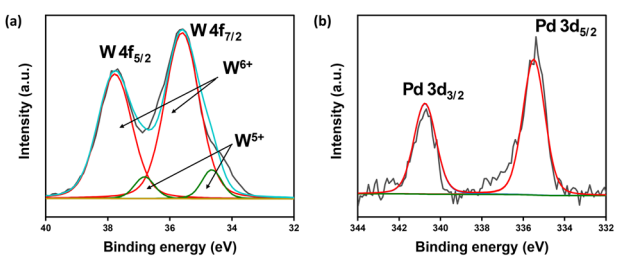

Fig. 5 (a) The W 4f and (b) Pd 3d XPS spectrum of Pd colloids/WO_{3-x}.

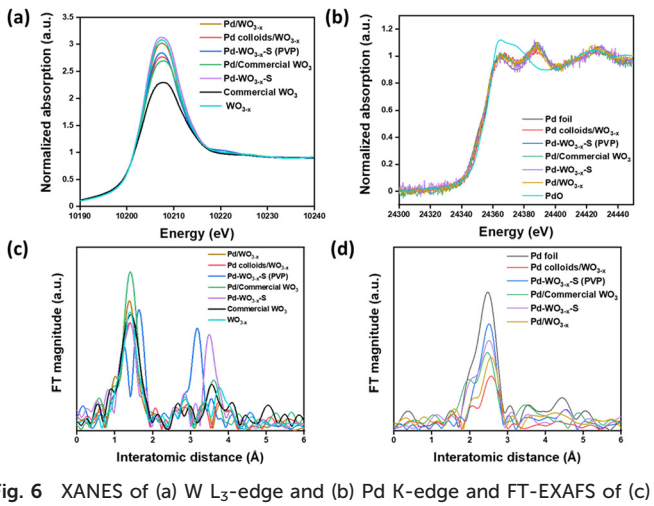

Fig. 6 XANES of (a) W L_3-edge and (b) Pd K-edge and FT-EXAFS of (c) W L_3-edge (d) Pd K-edge for prepared samples.

explored for the catalytic reduction of 4-NP into 4-AP.[56,58] Herein, we used the catalytic conversion of 4-NP to 4-AP (Fig. 7a) as a model reaction to evaluate the catalytic activity in the presence and absence of light irradiation. AB was used as the source of *in situ* hydrogen generation due to its high stability, non-toxic nature, and ease of handling, offering a safer and more sustainable alternative.[59]

Fig. 7(b and c) illustrates the kinetics of the catalytic conversion for the catalytic reduction of 4-NP to 4-AP in dark and light irradiation conditions, plotted as $-\ln(C/C_0)$ *versus* time, where C_0 denotes the initial concentration of 4-NP, while C refers to its concentration at a given reaction time. The reduction efficiency varied with the nature of the catalyst employed, highlighting the significance of structural properties and material composition on the catalytic performance. The reaction rate in dark conditions (Fig. 7(b)) follows the order: Pd colloids/WO_{3-x} > Pd/WO_{3-x} > Pd/Commercial WO_3. Pd-WO_{3-x}-S and Pd-WO_{3-x}-S (PVP) prepared *via* the solvothermal method did not show any catalytic activity. Also, bare WO_{3-x} and commercial WO_3 were inactive in this reaction. The hydrogen evolution in the dark arises solely from the catalytic contributions of Pd and defect-rich WO_{3-x}. In this system, Pd acts as the primary active site for AB decomposition due to its well-known intrinsic catalytic activity under dark conditions. The hydrogenation of 4-NP predominantly occurs on Pd NPs, where activated hydrogen is transferred to the nitro group. Fig. 7(d) shows that WO_{3-x} alone is inactive for 4-NP reduction, while Pd/WO_{3-x} exhibits a much faster reaction rate. This confirms that Pd acts as the hydrogen-activating site. Metallic Pd^0 dissociates H_2 or forms surface hydrides, which transfer hydrogen to the $-NO_2$ group, enabling efficient conversion of 4-NP to 4-AP.[60]

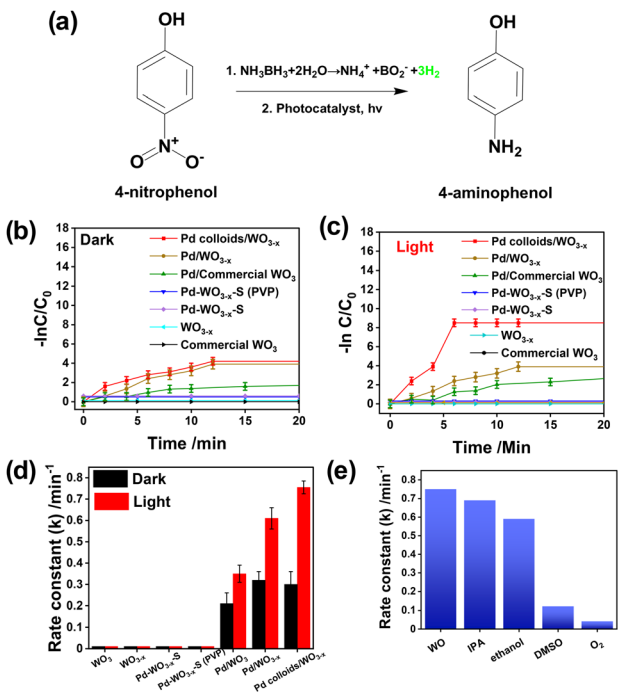

Fig. 7 (a) Photocatalytic reduction reaction of 4-NP to 4-AP, employing AB as a hydrogen source under visible-light irradiation, (b) time-course kinetic profile of 4-NP to 4-AP under dark conditions, (c) under light irradiation conditions, (d) comparison of rate constant in dark and under light irradiation, (e) effect of different scavengers on the rate constant under light irradiation. Reaction conditions: 5 mg catalyst, 10 mL water, 7 mM 4-NP, 5 mL of 0.025 M AB solution, and 300 W Xenon lamp.

The same trend in the catalytic performance with enhanced reaction rates was obtained under light irradiation, as shown in Fig. 7(c).

The reaction was assumed to follow pseudo-first-order kinetics. The rate constant (min^{-1}) under light irradiation follows the order (Pd colloids/WO_{3-x} (0.75) > Pd/WO_{3-x} (0.61) > Pd/commercial WO_3 (0.35)). Under dark conditions, the corresponding values are 0.30, 0.32, and 0.21 for Pd colloids/WO_{3-x}, Pd/WO_{3-x}, and Pd/Commercial WO_3, respectively. The comparison of the reaction rate constant in dark and light irradiation is shown in Fig. 7(d). From the obtained values, we conclude that the catalyst prepared *via* the impregnation method shows significantly higher activity in comparison to the solvothermal method. The sample prepared *via* the solvothermal method using PVP surfactant (Pd-WO_{3-x}-S (PVP)) and without using surfactant (Pd-WO_{3-x}-S), showed no observable activity either in dark or light irradiation conditions. The XPS analysis of these samples shows a very weak Pd signal, indicating that only a small amount of Pd is exposed on the surface. This limits the exposed Pd sites, resulting in poor catalytic activity. The kinetics of catalysis in dark and under light irradiation conditions measured *via* UV-vis absorption for the most active sample, Pd colloids/WO_{3-x}, are shown in Fig. S8.

We expect that the impregnation method facilitated a more uniform distribution of metal NPs on the photocatalyst support, enhancing active sites for the reaction. In contrast, the solvothermal method, especially when performed in the presence of surfactant, may partially encapsulate active metal NPs, limiting their accessibility during the reaction. Moreover, the solvothermal conditions often lead to the formation of larger-sized/agglomerated particles that subsequently reduce surface area and catalytic efficiency. Additionally, catalysts prepared by impregnation tend to exhibit better metal-support interaction, promoting effective separation of photogenerated charge carriers. Overall, the structural and morphological advantages achieved by the impregnation method provide a more favourable system, leading to improved conversion efficiency in the reduction of 4-NP.

Commercial WO_3 has a wide band gap with limited visible-light absorption, whereas WO_{3-x} shows band-gap narrowing due to oxygen vacancies, which introduce defects, extend visible-light absorption, and act as electron traps that suppress recombination and enhance electron transfer. The increased surface electron density also improves 4-NP adsorption and activation. Pd nanoparticles serve as an active site and facilitate catalytic reaction by acting as an electron sink, enabling rapid transfer of photogenerated electrons from WO_{3-x} and promoting strong charge separation.

The photocatalytic activity of Pd colloids/WO_{3-x} with 1.0, 2.5, and 5.0 wt% Pd was also investigated (Fig. S9). The 2.5 wt% sample showed much faster reaction rate than 1.0 wt%, confirming that additional Pd sites enhance electron trapping and accelerate reaction kinetics. At 5.0 wt%, the activity became extremely rapid, completing the reaction within 5 minutes in the dark and 2 minutes under light irradiation conditions, making kinetic analysis difficult. These results clearly demonstrate that increasing the Pd loading steadily enhances both dark and light-driven reduction pathways. Table S2 provides a comparative overview of reported plasmonic photocatalysts and their kinetic performance toward 4-NP reduction, enabling direct assessment of their relative catalytic efficiencies.

To identify the reactive species that drive the conversion of 4-NP reduction to 4-AP over Pd-colloids/WO_{3-x} catalyst, a systematic scavenger study was performed. All reactions were carried out under the standard conditions as described earlier, with the addition of 2.5 mM of scavenger. As illustrated in Fig. 7(e), without using any scavenger, the reaction rate was not affected. However, by adding a hydroxyl radical scavenger, isopropanol (IPA), the reaction rate was not much affected, suggesting ·OH radicals may contribute to the reaction, but are not the dominant species. Ethanol, a hole scavenger, led to a noticeable decrease in the rate, indicating that photogenerated holes indirectly affect the reaction by influencing charge recombination dynamics. In contrast, a significant decrease in the reaction rate was observed with the addition of electron scavengers, DMSO and O_2. These findings confirm that photogenerated electrons are the dominant species driving 4-NP reduction, while the ·OH radicals and holes play supportive roles.[61,62]

To investigate the structural and morphological changes leading to catalyst deactivation, an increased amount of catalyst (20 mg instead of the standard 5 mg) was used in subsequent cycles under the same reaction conditions as shown in Fig. 8(a). After each cycle, nitrogen gas was introduced into the reactor for 10 min to eliminate the hydrogen generated from AB. The catalyst was not separated or washed; instead, fresh 4-NP and AB solutions were added directly to the existing catalyst suspension to initiate the next cycle. The reaction was repeated under the same conditions for three cycles. The catalytic activity was maintained up to two cycles, and a decrease in activity was observed in the third cycle, indicating catalyst deactivation. The gradual decrease in activity may be due to changes on the catalyst surface, such as nanoparticle aggregation or surface blocking. The post-reaction characterization using XRD and TEM was carried out to examine the crystal structure and morphological changes after recycling, as shown in Fig. 8(b–d). XRD analysis Fig. 8(b) confirmed that the monoclinic phase of WO_{3-x} is preserved after the reaction, indicating structural stability. However, impurity peaks were also observed, probably due to the formation of by-products during the catalytic process. The TEM images before the reaction (Fig. 8(c)) exhibit a loosely arranged nanorod morphology with uniformly dispersed Pd NPs. After the reaction (Fig. 8(d)), the nanorods transform into more densely packed aggregates. This morphological change may reduce surface accessibility and hinder mass transport, potentially impacting catalytic performance.

The reduction of 4-NP facilitated by Pd colloids/WO_{3-x} in the presence of AB proceeds through a synergistic photocatalytic pathway involving light absorption, hydrogen generation, and selective hydrogen transfer, as illustrated in Scheme 1(a). The photocatalytic efficiency arises from the readily accessible active Pd metal sites. The reduction of 4-NP proceeds through two key steps: (1) the mildly basic ammonia borane converts 4-NP to the nitrophenolate ion, forming a stable intermediate; and (2) the nitrophenolate ion is subsequently reduced to 4-AP on the catalyst surface, as illustrated in Scheme 1(a). Hydrogen generated *in situ* from ammonia borane is transferred to the adsorbed nitrophenolate species, reducing the nitro group to an amino group, after which 4-AP desorbs from the catalyst surface. Additionally, these reactive hydrogen species may synergistically interact with photogenerated electrons originating from WO_{3-x}, contributing to the stepwise conversion of 4-NP to its 4-hydroxylaminophenol intermediate and finally to 4-AP.[61,63] The combined effects of

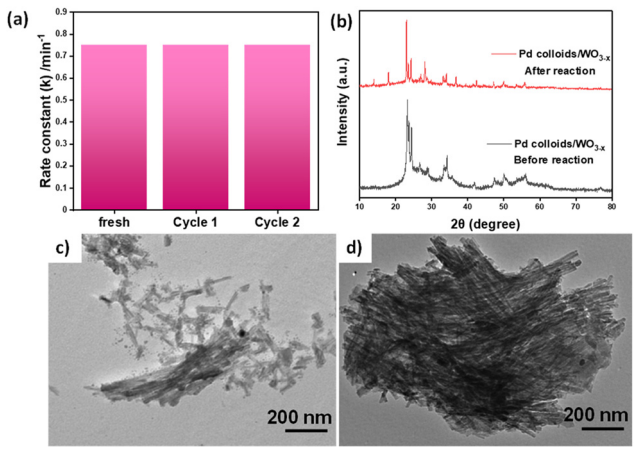

Fig. 8 (a) Reusability test under light illumination (b) XRD pattern of Pd colloids/WO_{3-x} before and after the reaction (c and d) TEM images of Pd colloids/WO_{3-x} before and after the reaction, respectively. Reaction conditions: 20 mg catalyst, 10 mL water, 7 mM 4-NP, 5 mL of 0.025 M AB solution, and 300 W Xenon lamp.

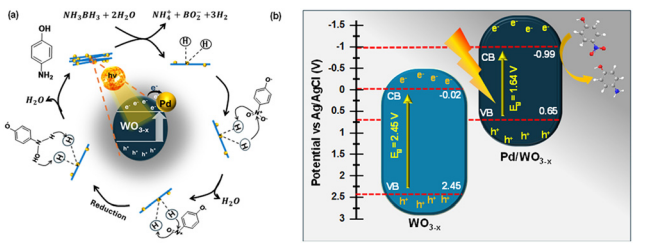

Scheme 1 (a) Plausible reaction pathway and (b) band alignment of WO_{3-x} and Pd/WO_{3-x} illustrating electron transfer under illumination, enabling efficient photoreduction of 4-NP.

oxygen vacancy-mediated charge separation, plasmonic electron trapping at Pd sites, under visible light irradiation make this catalytic system efficient.[49–51]

The Mott–Schottky plots provide the conduction band edge positions, which were found to be −0.11 V (WO_3), −0.02 V (WO_{3-x}), and −0.99 V (Pd colloids/WO_{3-x}) *vs.* Ag/AgCl. Using these values along with the experimentally determined band gaps (2.58 eV for WO_3, 2.45 eV for WO_{3-x}, and 1.64 eV for Pd colloids/WO_{3-x}), the valence band positions were calculated as +2.47 V, +2.45 V, and +1.64 V, respectively, as shown in Scheme 1(b). Importantly, the conduction band of Pd colloids/WO_{3-x} lies at −0.99 V, which is sufficiently negative to thermodynamically drive the reduction of 4-nitrophenol (−0.76 V to −0.80 V *vs.* Ag/AgCl).[64] This confirms that electron transfer from the Pd colloids/WO_{3-x} CB to nitrophenol is energetically feasible, whereas bare WO_3 and WO_{3-x} do not possess sufficiently negative CB positions. The significant CB shift and narrowed bandgap for Pd colloids/WO_{3-x} also indicate enhanced electron density and improved charge separation at the interface. Therefore, the inclusion of band-edge positions directly supports our proposed redox mechanism and validates the claim that Pd colloids/WO_{3-x} exhibits improved e^-/h^+ separation and is energetically favorable for nitrophenol reduction.[65]

Conclusions

In conclusion, Pd-deposited WO_{3-x} photocatalysts were prepared *via* impregnation and solvothermal methods by tuning their morphology (nanorods, nanosheets, and nanoblocks). The prepared catalysts were characterized by XRD, SEM, HR-TEM, XAS, BET, Mott Schottky, XPS, and EPR to examine the crystallographic structure, morphological variations, surface area characteristics, and the presence of oxygen defects. The defect-engineered WO_{3-x} showed an approximately 30 times enhancement in surface area compared to commercial WO_3, demonstrating the effectiveness of defect introduction. The UV-vis analysis revealed improved light absorption in the visible to near-infrared region. Among all catalysts, Pd colloids/WO_{3-x} and Pd/WO_{3-x} exhibited superior catalytic performance for the reduction of 4-NP, with higher values of reaction rate constant 0.75 min^{-1} and 0.61 min^{-1}, respectively, under light irradiation conditions. An approximate 2.5 times enhancement in the reaction rate was observed in comparison to dark conditions, with a reaction rate of 0.30 min^{-1} and 0.37 min^{-1} for Pd colloids/WO_{3-x} and Pd/WO_{3-x}, respectively. Additionally, the catalysts demonstrated stability and reusability in recycling tests. To understand the reaction mechanism, scavenger experiments were carried out, providing insight into the photocatalytic process. Overall, this work highlights the potential of Pd deposited oxygen-deficient WO_{3-x} nanomaterials, engineered through controlled morphology, for enhanced photocatalytic applications under broad-spectrum light irradiation.

Conflicts of interest

There are no conflicts to declare.

Data availability

The data supporting this article have been included as part of the supplementary information (SI).

Supplementary information: synthesis of colloidal Pd nanoparticles, thermogravimetric analysis, FT-IR spectra, XPS, Mott–Schottky and Tauc plot. Reaction kinetics for nitroaromatic reduction reaction. See DOI: https://doi.org/10.1039/d5cy01196e.

Acknowledgements

Priyanka Verma thanks the seed and matching equipment grant supported by IIT Delhi (MI03052; MI03068), CSIR-ASPIRE scheme (01WS(10)/2023-2024/EMRII/ASPIRE), and the Research Fund by the Royal Society of Chemistry (R24-1159911204) for the financial support. Priyanka (Ref. No. 231610046924) thanks UGC for the PhD fellowship. SY thanks the Japan Society for the Promotion of Science (JSPS) KAKENHI (No. 24H02217 in Transformative Research Areas (A) JP24A202 Integrated Science of Synthesis by Chemical Structure Reprogramming). The authors thank the Central Research Facility (CRF) and Nanoscale Research Facility (NRF) at IIT Delhi for providing access to research infrastructure. XAFS measurements were performed at SPring-8 (Proposal number 2025A1655).

References

1 P. Verma, Y. Kuwahara, K. Mori, R. Watanabe, C. Fukuhara and H. Yamashita, *Energy Fuels*, 2023, **37**, 17652–17666.
2 J. Barber, *Chem. Soc. Rev.*, 2009, **38**, 185–196.
3 A. K. Nayak and D. Pradhan, *J. Phys. Chem. C*, 2018, **122**, 3183–3193.
4 H. Robatjazi, S. M. Bahauddin, C. Doiron and I. Thomann, *Nano Lett.*, 2015, **15**, 6155–6161.
5 S. Linic, P. Christopher and D. B. Ingram, *Nat. Mater.*, 2011, **10**, 911–921.
6 J. Lee, S. Mubeen, X. Ji, G. D. Stucky and M. Moskovits, *Nano Lett.*, 2012, **12**, 5014–5019.
7 J. A. Faucheaux, A. L. D. Stanton and P. K. Jain, *J. Phys. Chem. Lett.*, 2014, **5**, 976–985.
8 P. Verma, K. Mori, Y. Kuwahara, R. Raja and H. Yamashita, *Mater. Adv.*, 2021, **2**, 880–906.
9 R. Jiang, B. Li, C. Fang and J. Wang, *Adv. Mater.*, 2014, **26**, 5274–5309.
10 S. Luo, X. Ren, H. Lin, H. Song and J. Ye, *Chem. Sci.*, 2021, **12**, 5701–5719.
11 E. Petryayeva and U. J. Krull, *Anal. Chim. Acta*, 2011, **706**, 8–24.
12 S. J. A. Moniz, S. A. Shevlin, D. J. Martin, Z. X. Guo and J. Tang, *Energy Environ. Sci.*, 2015, **8**, 731–759.
13 S. Vikal, Y. K. Gautam, S. Meena, V. Parewa, A. Kumar, S. Meena, S. Kumar and B. P. Singh, *Nanoscale Adv.*, 2023, **5**, 805–819.

14 D. Chen, Y. Cheng, N. Zhou, P. Chen, Y. Wang, K. Li, S. Huo, P. Cheng, P. Peng, R. Zhang, L. Wang, H. Liu, Y. Liu and R. Ruan, *J. Cleaner Prod.*, 2020, **268**, 121725.
15 A. Zarei, F. Hedayatinasab and H. Rezaei-Vahidian, *Environ. Prog. Sustainable Energy*, 2020, **39**, e13386.
16 S. Nishimoto, T. Mano, Y. Kameshima and M. Miyake, *Chem. Phys. Lett.*, 2010, **500**, 86–89.
17 S. Singh, S. Parveen, L. Clarizia and P. Kumar, *Catal. Rev.: Sci. Eng.*, 2025, 1–49.
18 L. Wang, X. Xu, Z. Feng, L. Bian and Y. Wang, *J. Solid State Chem.*, 2018, **266**, 23–30.
19 Y. Huang, Y. Yu, Y. Yu and B. Zhang, *Sol. RRL*, 2020, **4**, 2000037.
20 K. Pan, K. Shan, S. Wei, K. Li, J. Zhu, S. H. Siyal and H. H. Wu, *Compos. Commun.*, 2019, **16**, 106–110.
21 J. Chen, S. Shen, P. Guo, M. Wang, J. Su, D. Zhao and L. Guo, *J. Mater. Res.*, 2014, **29**, 64–70.
22 T. Paik, M. Cargnello, T. R. Gordon, S. Zhang, H. Yun, J. D. Lee, H. Y. Woo, S. J. Oh, C. R. Kagan, P. Fornasiero and C. B. Murray, *ACS Energy Lett.*, 2018, **3**, 1904–1910.
23 L. Zhang, H. Wang, J. Liu, Q. Zhang and H. Yan, *J. Mater. Sci.: Mater. Electron.*, 2020, **31**, 861–873.
24 H. Quan, Y. Gao and W. Wang, *Inorg. Chem. Front.*, 2020, **7**, 817–838.
25 Q. Liu, F. Wang, H. Lin, Y. Xie, N. Tong, J. Lin, X. Zhang, Z. Zhang and X. Wang, *Catal. Sci. Technol.*, 2018, **8**, 4399–4406.
26 H. Yin, Y. Kuwahara, K. Mori, H. Cheng, M. Wen, Y. Huo and H. Yamashita, *J. Phys. Chem. C*, 2017, **121**, 23531–23540.
27 H. Cheng, T. Kamegawa, K. Mori and H. Yamashita, *Angew. Chem., Int. Ed.*, 2014, **53**, 2910–2914.
28 S. Meena, M. Sethi, S. Meena, P. Saini, K. Kumar, S. Saini, S. Shekhawat, M. L. Meena, A. Dandia, S.-D. Lin and V. Parewa, *Environ. Res.*, 2023, **231**, 116181.
29 Z. Lou, Q. Gu, Y. Liao, S. Yu and C. Xue, *Appl. Catal., B*, 2016, **184**, 258–263.
30 Dimple, Priyanka, R. Watanabe, C. Fukuhara, H. Yamashita and P. Verma, *Catal. Sci. Technol.*, 2024, **14**, 4775–4798.
31 G. Xi, S. Ouyang, P. Li, J. Ye, Q. Ma, N. Su, H. Bai and C. Wang, *Angew. Chem., Int. Ed.*, 2012, **51**, 2395–2399.
32 C. M. Wu, S. Naseem, M. H. Chou, J. H. Wang and Y. Q. Jian, *Front. Mater.*, 2019, **6**, 00049.
33 P. Verma, Y. Kuwahara, K. Mori and H. Yamashita, *Catal. Sci. Technol.*, 2017, **7**, 2551–2558.
34 M. Navlani-Garcia, M. Martis, D. Lozano-Castello, D. Cazorla-Amoros, K. Mori and H. Yamashita, *Catal. Sci. Technol.*, 2015, **5**, 364–371.
35 M. Navlani-Garcia, K. Mori, A. Nozaki, Y. Kuwahara and H. Yamashita, *ChemistrySelect*, 2016, **1**, 1879–1886.
36 T. Song, F. Gao, S. Guo, Y. Zhang, S. Li, H. You and Y. Du, *Nanoscale*, 2021, **13**, 3895–3910.
37 H. Asakura, S. Yamazoe, T. Misumi, A. Fujita, T. Tsukuda and T. Tanaka, *Radiat. Phys. Chem.*, 2020, **175**, 108270.
38 Z. Lou, Q. Gu, L. Xu, Y. Liao and C. Xue, *Chem. – Asian J.*, 2015, **10**, 1291–1294.
39 Dimple, S. Pratap Singh, F. Amano, K. Beppu, R. Watanabe, C. Fukuhara and P. Verma, *ChemCatChem*, 2025, e00795.
40 Y. Lu, Y. Jiang, X. Gao, X. Wang and W. Chen, *J. Am. Chem. Soc.*, 2014, **136**, 11687–11697.
41 G. Hai, J. Huang, L. Cao, Y. Jie, J. Li, X. Wang and G. Zhang, *J. Alloys Compd.*, 2017, **690**, 239–248.
42 K. Zhang, Y. Li, Z. Fu, X. Chi, Y. Xiong, Y. Yao, X. Wang, Z. Tang, J. Wang, K. Nie, Z. Yang and Y. M. Yan, *ACS Appl. Mater. Interfaces*, 2023, **15**, 15024–15035.
43 W. Q. Zhao, Q. Zhao, Z. K. Song, L. Ma, X. B. Chen, S. J. Ding and L. Zhou, *ACS Appl. Nano Mater.*, 2022, **5**, 16440–16450.
44 K. Shi, F. Wang, X. Li, W. Huang, K. Lu, C. Yu and K. Yang, *J. Mater. Sci.*, 2023, **58**, 16309–16321.
45 P. Gholami, A. Khataee and A. Bhatnagar, *J. Cleaner Prod.*, 2020, **275**, 124157.
46 P. Gholami, A. Khataee, A. Bhatnagar and B. Vahid, *ACS Appl. Mater. Interfaces*, 2021, **13**, 13072–13086.
47 F. Liu, X. Chen, Q. Xia, L. Tian and X. Chen, *RSC Adv.*, 2015, **5**, 77423–77428.
48 K. Kumar Das, D. P. Sahoo, S. Mansingh and K. Parida, *ACS Omega*, 2021, **6**, 30401–30418.
49 A. Jaryal, V. Rao Battula and K. Kailasam, *ACS Appl. Energy Mater.*, 2020, **3**, 4669–4676.
50 Y. Kong, H. Sun, W. Fan, L. Wang, H. Zhao, X. Zhao and S. Yuan, *RSC Adv.*, 2017, **7**, 15201–15210.
51 Y. Xia, X. Xia, S. Zhu, R. Liang, G. Yan, F. Chen and X. Wang, *Molecules*, 2023, **28**, 8013.
52 M. B. Cetin, T. Top, M. Yurderi, M. Zahmakıran and M. Rakap, *Int. J. Hydrogen Energy*, 2024, **72**, 60–73.
53 M. Takahashi, Y. Kitazaki, H. Oshima, M. Harada and S. Maenosono, *J. Phys. Chem. C*, 2023, **127**, 8175–8185.
54 A. Kuzmin, J. Purans and P. Parent, *J. Phys.: Condens. Matter*, 1993, **5**, 9423–9430.
55 Ajay, H. Jaipal, R. Watanabe, C. Fukuhara and P. Verma, *J. Chem. Sci.*, 2025, **137**, 14.
56 S. Maged, O. M. El-Borady, H. El-Hosainy and M. El-Kemary, *Environ. Sci. Pollut. Res.*, 2023, **30**, 117909–117922.
57 H. Zhang, Q. Niu, Y. Mou, Z. Bian, T. Zhang, C. Chu, D. Han, F. Wang, G. Wang and L. Bing, *J. Environ. Chem. Eng.*, 2025, **13**, 115936.
58 Z. Yuan, X. Wang, Y. Liu, P. Zhou and R. Y. Liu, *React. Chem. Eng.*, 2025, **10**, 953–958.
59 P. Verma, M. Navlani-García, Y. Kuwahara, K. Mori and H. Yamashita, *J. Chem. Sci.*, 2017, **129**, 1661–1669.
60 B. D. Adams and A. Chen, *Mater. Today*, 2011, **14**, 6.
61 S. Velusamy, A. Roy, E. Mariam, S. Krishnamurthy, S. Sundaram and T. K. Mallick, *Sci. Rep.*, 2023, **13**, 1.
62 G. Naresh and T. K. Mandal, *ACS Appl. Mater. Interfaces*, 2014, **6**, 21000–21010.
63 N. C. Para, A. Raj and M. Haukka, *Nano Sel.*, 2025, e70074.
64 A. K. Samuel, Z. Ertekin, B. Moses Abraham, Z. Yang, M. D. Symes and A. Y. Ganin, *Dalton Trans.*, 2025, **54**, 16525–16534.
65 M. Ismael, *J. Photochem. Photobiol., A*, 2023, **439**, 114576.